Research Square

Preprints are preliminary reports that have not undergone peer review.
They should not be considered conclusive, used to inform clinical practice,
or referenced by the media as validated information.

Optimization of microstructure and electrical properties of ZnO-Cr2O3-based varistors by Tm2O3 doping

Wenbin Cao

caowenbin@sust.edu.cn

Shaanxi University of Science and Technology

Huitao Wang

Shaanxi University of Science and Technology

Chenyuan Gou

Shaanxi University of Science and Technology

Xinyao Wang

Shaanxi University of Science and Technology

Jianke Liu

Shaanxi University of Science and Technology

Mingxia Li

Shaanxi University of Science and Technology

Research Article

Keywords: Zinc oxide, Varistors, Tm2O3 doping, Electrical properties, Grain boundary barrier

Posted Date: July 13th, 2026

DOI: https://doi.org/10.21203/rs.3.rs-10127443/v1

License: This work is licensed under a Creative Commons Attribution 4.0 International License.
Read Full License

Additional Declarations: No competing interests reported.

Optimization of microstructure and electrical properties of ZnO-Cr_2O_3-based varistors by Tm_2O_3 doping

Wenbin Cao*, Huitao Wang, Chenyuan Gou, Xinyao Wang, Jianke Liu, Mingxia Li

Research Center for Semiconductor Materials and Devices, Shaanxi University of Science and Technology, Xi'an 710021, China

Abstract

ZnO varistors are essential components for voltage protection in the power industry. With the growing demand for miniaturized electronic devices, the development of varistors with a high voltage gradient is of great importance. In this work, ZnO-Cr_2O_3-based varistors doped with Tm_2O_3 were prepared, and the relationship between their microstructure and electrical properties was analyzed. The results indicate that as the Tm_2O_3 doping content increases from 0.00 to 0.50 mol%, a portion of Tm^{3+} ions incorporate into the ZnO lattice, substituting for Zn^{2+}, while the excess Tm_2O_3 is segregated at the grain triple junctions. The secondary phase Tm_2O_3 pins the grain boundary migration and inhibits grain growth, leading to a more uniform grain size distribution and a reduction in the average grain size from 3.16 to 1.37 μm. The increased number of grain boundaries per unit thickness resulted in a remarkable enhancement of the voltage gradient strength E_{1mA} from 428.37 to 1778.33 V/mm. Concurrently, the synergistic enrichment of the Tm_2O_3 phase and Co element at the grain boundaries effectively increases the interface state density N_S, which in turn raises the grain boundary barrier height φ_b from 0.2 to 0.66 eV. The enhanced barrier height significantly improves the blocking effect on charge carriers, leading to a substantial increase in the nonlinear coefficient α from 6.22 to 54.36 and a reduction in the leakage current density J_L from 375.75 to 0.97 μA/cm². However, when the doping level exceeds 0.50 mol%, excessive Tm_2O_3 segregation causes an inhomogeneous distribution of the grain boundary phase, triggering abnormal grain growth and a decrease in barrier height, which ultimately degrades the overall electrical performance. This study demonstrates that optimal Tm_2O_3 doping (0.50 mol%) is an effective strategy for achieving ZnO-Cr_2O_3-based varistors with a high voltage gradient, high nonlinear

* Corresponding author. E-mail: caowenbin@sust.edu.cn

coefficient, and low leakage current through combined grain refinement and grain boundary engineering.

Keywords: Zinc oxide; Varistors; Tm_2O_3 doping; Electrical properties; Grain boundary barrier

1 Introduction

ZnO varistors, renowned for their excellent nonlinear current-voltage characteristics and surge absorption capacity, are core components for overvoltage protection in power systems and electronic devices [1-3]. Their unique nonlinear behavior originates from the formation of double Schottky barriers (DSBs) at the grain boundaries (GBs), where segregated dopants create atomic-level defect structures [4]. Since the initial investigation into the nonlinear characteristics of ZnO-TiO_2 varistors, significant research has been devoted to enhancing the electrical properties of ZnO-based varistors [5]. It has been established that doping pure ZnO with multi-component metal oxides, such as Bi_2O_3, CoO, and MnO, imparts excellent nonlinear electrical characteristics.

Recently, a novel ZnO-Cr_2O_3-based varistor ceramic system has been developed, overcoming issues associated with conventional systems like Bi_2O_3 vaporization in ZnO-Bi_2O_3, or the use of expensive or toxic rare-earth elements in ZnO-Pr_6O_{11} and ZnO-V_2O_5 systems [6-8]. Tian et al. reported that ZnO-Cr_2O_3-based varistors co-doped with Ca, Co, and Sb oxides exhibits a superior nonlinear coefficient α of 219, a low leakage current density below 0.20 μA/cm^2, and a voltage gradient of 925 V/mm [9]. In subsequent work, they demonstrated that Cr_2O_3-doped ZnO-Cr_2O_3-based varistors achieves an α value of 73, a leakage current density of 0.20 μA/cm^2, and a voltage gradient of 383 V/mm [10].

Among rare-earth oxides, the effect of Tm_2O_3 doping on ZnO varistors, particularly within the ZnO-Cr_2O_3-based system, remains largely unexplored. Given the significantly larger ionic radius of Tm^{3+} (0.094 nm) compared to Zn^{2+} (0.074 nm) [11], it is anticipated that Tm^{3+} will be preferentially segregated at the grain boundaries, inhibiting grain boundary migration and suppressing ZnO grain growth, thereby providing a strategy to enhance the voltage gradient.

In this work, we systematically investigated the influence of Tm_2O_3 doping on the microstructure and electrical properties of ZnO-Cr_2O_3-based varistors. The relationship between microstructure and electrical performance was elucidated through comprehensive analyses of phase, morphology, and electrical characterization. The results demonstrate that Tm_2O_3 doping effectively

refines the ZnO grain, significantly enhances the voltage gradient and nonlinear coefficient, and substantially suppresses the leakage current, providing valuable insights for developing miniaturized varistors for highly integrated electronic systems.

2 Experimental procedure

2.1 Sample preparation

Samples with the nominal composition (97.40-x) mol% ZnO + 0.10 mol% Cr_2O_3 + 0.50 mol% Co_3O_4 + 2.00 mol% $CaCO_3$ + x mol% Tm_2O_3 (where x = 0.00, 0.25, 0.50, 0.75, 1.00) were synthesized via a conventional solid-state reaction route. Reagent-grade powders were weighed according to the stoichiometric ratio and mixed with 4 wt% polyvinyl alcohol (PVA) solution, deionized water, and zirconia grinding balls in a mass ratio of 1:0.4:1.6:4. The mixture was ball-milled in a planetary ball mill at 10 r/s for 5 h. The resulting slurry was dried at 90 °C for 8 h, manually ground, and sieved through a 120-mesh sieve (aperture size: 125 μm). The powder was uniaxially pressed into green bodies with a diameter of 8.0 mm and a thickness of 0.8 mm under a pressure of 420 MPa. The green bodies were heated in a sintering furnace at a heating rate of 3 °C/min to 600 °C and held for 5 h to remove the binder. They were subsequently heated at the same rate to 1100 °C, held for 3 h, and finally furnace-cooled to room temperature to obtain the sintered ZnO varistor samples. The sintered pellets were polished, and silver electrodes were applied on both surfaces by firing silver paste at 600 °C for 10 min.

2.2 Microstructure characterization

The phase composition of the samples was analyzed using an X-ray diffractometer (XRD, Rigaku-D/Max-2200PC, Japan) with Cu-Kα radiation, scanned over a 2θ range of 20 to 80°. The sample surfaces were polished and thermally etched at 1000 °C for 10 min, followed by morphological characterization using a scanning electron microscope (SEM, FEI Q45, USA). Elemental distribution was analyzed using energy-dispersive spectroscopy (EDS). Grain size distribution histograms and the average grain size d were obtained by statistically analyzing the size of over 100-200 ZnO grains from multiple regions of the SEM images.

2.3 Electrical properties measurement

The nonlinear coefficient α is a key parameter describing the varistor performance. A higher α indicates better performance. The electric field strength-current density (E-J) characteristics of

the samples were measured at 298.15 K using a high-voltage source meter (Keithley 2410, USA). The nonlinear coefficient α was calculated using Eq. 1 [18-21]:

$$\alpha = \frac{1}{\log(E_2 / E_1)} \tag{1}$$

where E_1 and E_2 are the electric field strengths at current densities of 0.1and 1.0 mA/cm²,respectively [22]. E_2 represents the voltage gradient E_{1mA}. The leakage current I_L was measured at an electric field strength of 0.75 E_2, and the leakage current density J_L was calculated using Eq. 2:

$$J_L = I_L / S \tag{2}$$

where S is the cross-sectional area of the sample.

The grain boundary barrier height φ_b was determined using the *J-E-T* testing method. This method involves measuring the *E-J* characteristics of the sample within a temperature range of 313.15–423.15 K to calculate the grain boundary barrier height φ_b, interface state density N_S, donor concentration N_D, and depletion layer width ω [23]. This approach is advantageous for its accuracy, non-destructiveness, and wide applicability [18, 19, 20, 24-27]. When the applied electric field is lower than E_{1mA}, the conduction mechanism in ZnO varistors is primarily governed by electron thermionic emission. The double Schottky barrier height φ_b is calculated based on the *E-J* characteristic Eq. 3, where β is defined by Eq. 4. Taking the logarithm of Eq. 3 yields Eq. 5. From Eq. 5, the ln*J* versus $E^{1/2}$ curves at different temperatures can be plotted. The constant β is obtained by linear fitting of these curves. The intercept at $E = 0$ in the ln*J*-$E^{1/2}$ plot gives lnJ_0. The relationship between lnJ_0 and 1000/T is then plotted according to Eq. 6 [18, 19, 20, 24-27].

$$J = AT^2 \exp(-\frac{\varphi_b - \beta E^{\frac{1}{2}}}{kT}) \tag{3}$$

$$\beta = \left[\left(\frac{1}{nt}\right)\left(\frac{2e^3}{4\pi\varepsilon_0\varepsilon_r}\right)\right]^{\frac{1}{2}} \tag{4}$$

$$\ln J = \ln(AT^2) - \frac{\varphi_b - \beta\sqrt{E}}{kT} \tag{5}$$

$$\ln J_0 = \ln(AT^2) - \frac{\varphi_b}{kT} \tag{6}$$

where A is the Richardson constant (1.20×10^{6} A/(m^2·K^2)), n is the number of grain boundaries along the sample thickness direction, e is the electron charge (1.602×10^{-19} C), ε_0 is the permittivity of vacuum(8.854×10^{-12} F/m), ε_r is the relative permittivity of ZnO (ε_r is a dimensionless number and has no international standard unit), k is the Boltzmann constant (1.38×10^{-23} J/K), and T is the absolute temperature.

This study measured the E-J characteristic data of the samples in the temperature range of 313.15–423.15 K. Within this range, the change of $\ln(AT^2)$ at different temperatures is relatively small and can be considered constant, as shown in Eq. 7. Therefore, the $\ln J_0$-$1000/T$ curve can be considered a straight line. The β value is substituted into Eq. 4 to calculate the depletion layer width ω on both sides of the grain boundary [18, 19, 26, 28, 29]. The slope is obtained by fitting the ln J_0-1000/T relationship diagram, and the barrier height φ_b can be calculated according to Eq. 6. The donor concentration N_D, interface state density N_S, and the value of N_S^2/N_D can be calculated according to Eqs. 8 and 9.

$$\frac{\ln 423.15}{\ln 313.15}=1.0523 \tag{7}$$

$$N_S=\left(\frac{2\varepsilon_0\varepsilon_r N_D\varphi_b}{e^2}\right)^{\frac{1}{2}} \tag{8}$$

$$t=\frac{N_S}{N_D} \tag{9}$$

3 Results and discussion

3.1 Phase and morphology

Fig. 1a shows the XRD patterns of the samples with different Tm_2O_3 contents. The results indicate the presence of only two phases: the primary ZnO phase (PDF: 99-0111) and a minor Tm_2O_3 phase (PDF: 41-1090). The undoped sample consists predominantly of the ZnO phase. When the Tm_2O_3 content is ≥ 0.25 mol%, the intensity and number of diffraction peaks corresponding to the Tm_2O_3 phase gradually increase with increasing dopant concentration. No phases related to Cr_2O_3, Co_3O_4, or $CaCO_3$ are detected, likely because their concentrations are below the XRD detection limit.

Fig. 1b presents an enlarged view of the XRD patterns in the 2θ range of 33.5–37°. When the Tm_2O_3 doping level is 0.25 mol%, the diffraction peaks of the ZnO phase shift significantly towards

lower angles. According to Bragg's law (Eq. 10), an increase in the interplanar spacing d_1 leads to a decrease in the diffraction angle θ, resulting in a peak shift to lower angles [30]:

$$2d_1 \sin\theta = n\lambda \tag{10}$$

where θ is the diffraction angle, d_1 is the interplanar spacing, and λ is the X-ray wavelength. The ionic radius of Tm^{3+} (0.099 nm) is larger than that of Zn^{2+} (0.074 nm). The substitution of Tm^{3+} for Zn^{2+} in the ZnO lattice increases the lattice constant and interplanar spacing, causing the observed peak shift. As the Tm_2O_3 content increases beyond 0.25 mol%, the position of the ZnO peaks remains unchanged, suggesting that the solid solubility limit of Tm^{3+} in the ZnO grains is reached at approximately 0.25 mol%.

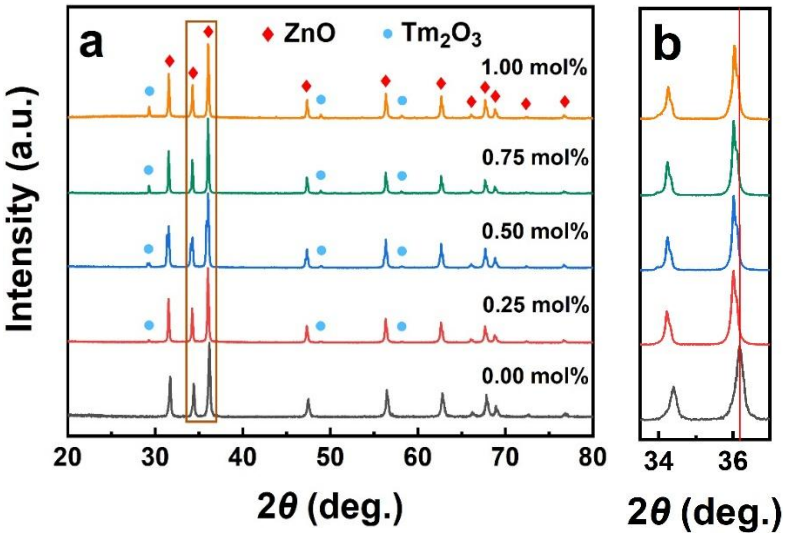


Fig. 1 (a) XRD patterns of the samples with different Tm_2O_3 contents. (b) Enlarged XRD patterns of 33.5-37° in (a).

Figs. 2a-e display the SEM images and corresponding log-normal grain size distribution histograms for the samples with different Tm_2O_3 concentrations. Fig. 2f shows the relationship between Tm_2O_3 content and the average grain size d. The microstructure primarily consists of ZnO grains and a small amount of secondary phase enriched at the triple junctions. Combined with XRD analysis, as the Tm_2O_3 content increases, Tm^{3+} ions are predominantly segregated at the ZnO grain boundaries as a Tm_2O_3 phase, creating a Zener pinning effect that inhibits grain boundary migration and grain growth. As shown in Fig. 2c, when the Tm_2O_3 content reaches 0.50 mol%, the Tm_2O_3 phase forms uniformly aggregated clusters at the triple junctions, effectively limiting ZnO grain growth. The average grain size d decreases to 1.37 μm, and the size distribution becomes more uniform. However, as shown in Fig. 2e, when the Tm_2O_3 content increases further to 1.00 mol%,

the grain size increases to 1.71 μm. This is attributed to the formation of significantly larger and unevenly distributed Tm_2O_3 clusters at the triple junctions.

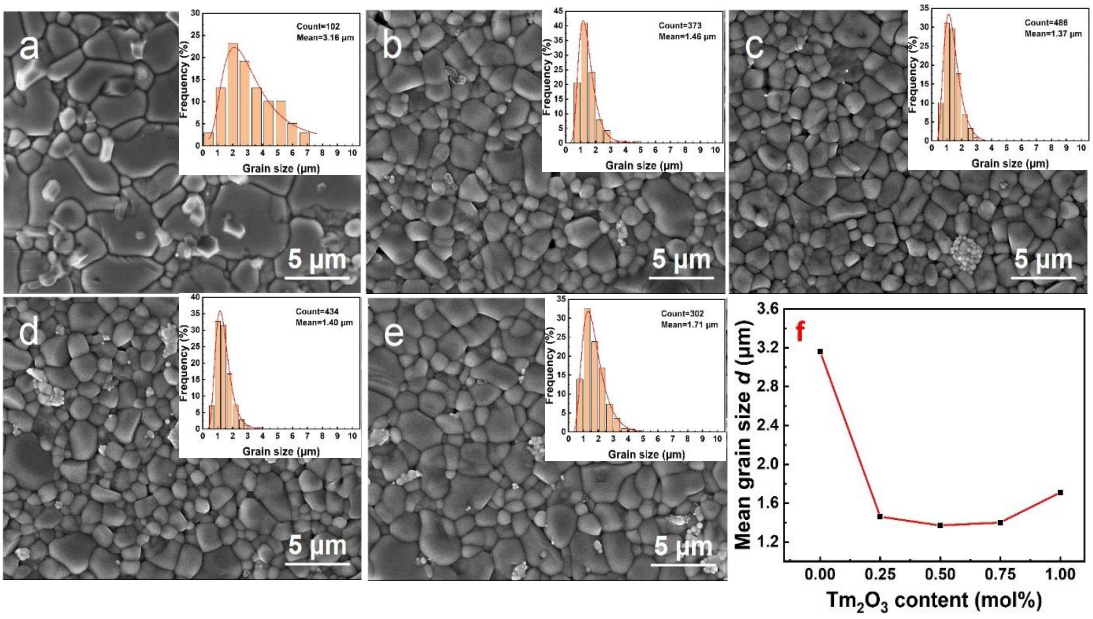


Fig. 2 SEM images and grain size distribution histograms of the samples with Tm_2O_3 contents of 0.00 mol% (a), 0.25 mol% (b), 0.50 mol% (c), 0.75 mol% (d), and 1.00 mol% (e). (f) The relationship between Tm_2O_3 content and average grain size.

Figs. 3 and 4 show the EDS elemental distribution mappings for the undoped sample and the sample doped with 0.50 mol% Tm_2O_3, respectively. In the undoped sample, Cr and Co elements are relatively uniformly distributed, while some Ca enrichment is observed at the grain boundaries. From Fig. 4, for the 0.50 mol% Tm_2O_3 sample, Cr and Ca elements remain uniformly distributed, whereas significant co-enrichment of Co and Tm elements is observed at the grain boundaries, with their enrichment regions overlapping. Fig.5 presents an EDS line scan across a grain boundary in the 0.50 mol% Tm_2O_3-doped sample, confirming that the distributions of Co and Tm are similar and both are enriched at the triple junctions. Combined with XRD analysis, it indicates that the Tm_2O_3 phase, which incorporates a substantial amount of Co, is distributed at the triple junctions of the ZnO grains, thereby modifying the grain boundary characteristics.

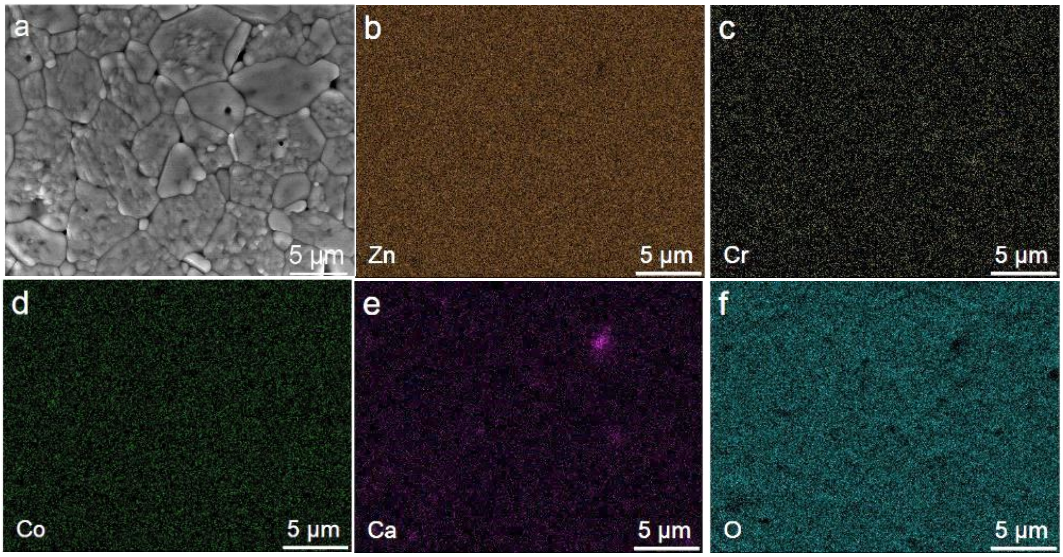


Fig. 3 SEM image and corresponding EDS elemental distribution mappings of the undoped sample.

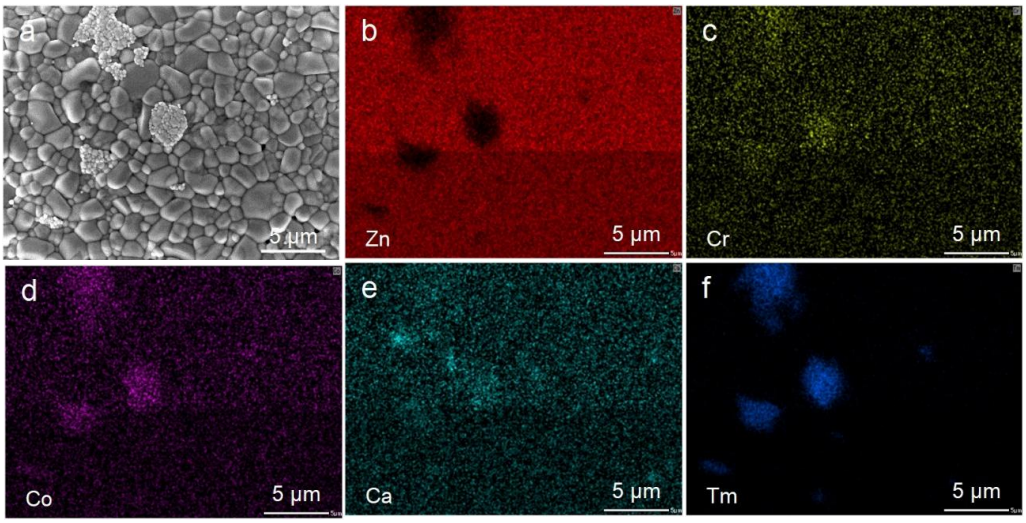


Fig. 4 SEM image and corresponding EDS elemental distribution maps of the sample with 0.50 mol% Tm_2O_3 doping.

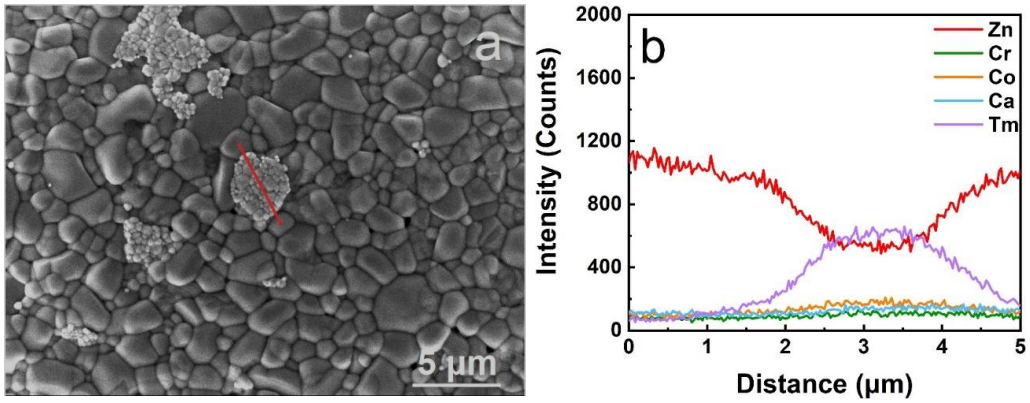


Fig. 5 (a) SEM image of the sample with 0.50 mol% Tm_2O_3. (b) EDS line scan profile of the underlined part in (a).

3.2 Electrical properties

The *E-J* characteristics of ZnO varistors exhibit non-ohmic behavior. The flatter the *E-J* characteristic curve after the inflection point, the better the nonlinear performance[36]. Fig. 6 shows the *E-J* characteristic curves and leakage current density J_L versus nonlinear coefficient α relationship for the samples with different Tm_2O_3 contents. The values of nonlinear coefficient α, voltage gradient E_{1mA}, and leakage current density J_L obtained from the *E-J* characteristics are shown in Table 1. From Fig.6b, it can be seen that as the Tm_2O_3 content increases, the nonlinear coefficient α first increases and then decreases, reaching a maximum at 0.50 mol%; the leakage current density J_L first decreases and then increases, reaching a minimum at 0.50 mol%. The sample with 0.50 mol% Tm_2O_3 exhibits the best electrical performance, with α = 54.36, E_{1mA} = 1778.33 V/mm, and J_L = 0.97 μA/cm².

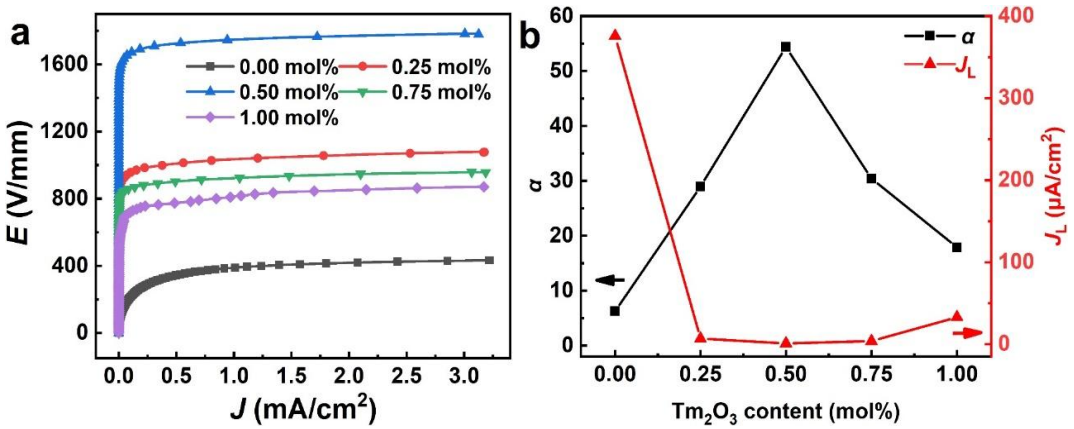


Fig. 6 *E-J* characteristic curves (a) and leakage current density J_L nonlinear coefficient α relationship diagram (b) for the samples with different Tm_2O_3 contents.

Table 1 Microstructure and electrical performance parameters of the samples with different Tm_2O_3 contents.

Tm_2O_3 (mol%)	d (μm)	α	$E_{1\ mA}$ (V/mm)	J_L (μA/cm²)
0.00	3.16	6.22	428.37	375.75
0.25	1.46	28.98	1073.96	6.89
0.50	1.37	54.36	1778.33	0.97
0.75	1.40	30.40	955.29	3.84
1.00	1.71	17.89	865.89	32.99

3.3 Double schottky barrier analysis

The significant improvement in the electrical properties of ZnO varistors is closely related to the change in the double Schottky barrier height φ_b [18, 19]. Fig.7 shows the ln J_0-1000/T relationship diagrams for the ZnO varistor samples with different Tm_2O_3 contents. The calculated values of barrier height φ_b, donor concentration N_D, and interface state density N_S are shown in Table 2. The results show that as the Tm_2O_3 content increases, the barrier height φ_b first increases and then decreases. The variation trend of the barrier height φ_b is consistent with the nonlinear coefficient α and opposite to the leakage current density J_L. The increase in barrier height makes it more difficult for electrons to overcome the barrier, leading to an opposite trend in leakage current density J_L compared to the barrier height φ_b. According to Eq. 8, the change in barrier height φ_b is related to the donor concentration N_D and interface state density N_S, i.e., φ_b is proportional to N_S^2/N_D. Fig.8 shows the relationship between φ_b and N_S^2/N_D for different Tm_2O_3 contents. It can be seen that as the Tm_2O_3 content increases, the trend of N_S^2/N_D is consistent with that of φ_b. However, observing the data in Table 2, the trend of φ_b is also the same as the individual trends of N_S and N_D. Therefore, the interface state density N_S has a more significant impact on the barrier height φ_b.

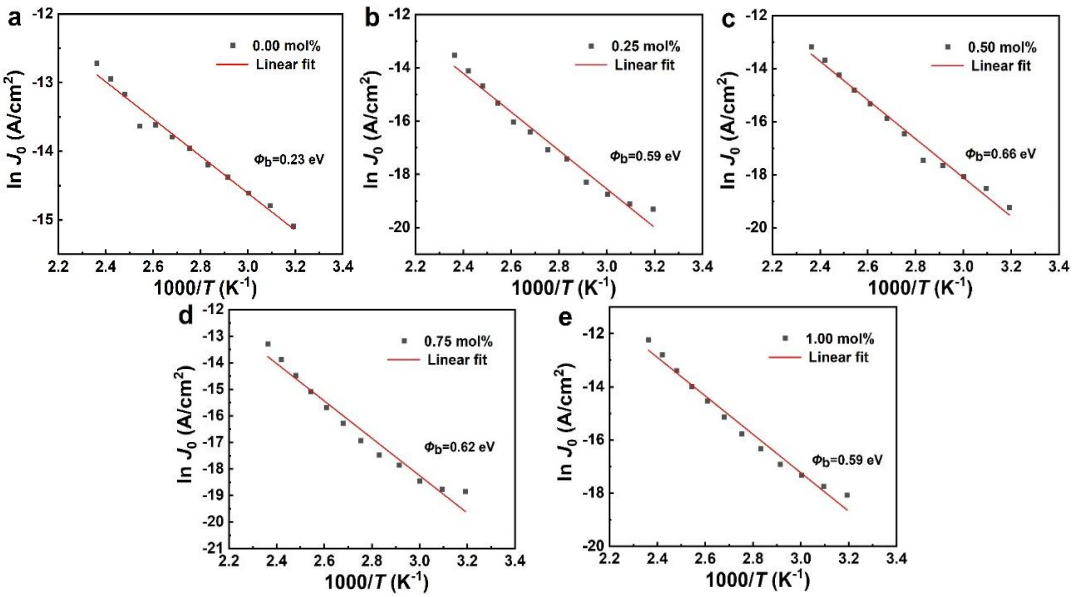


Fig. 7 lnJ_0-1000/T fitting curves for the samples with different Tm_2O_3 contents of 0.00-1.00 mol% (a-e).

According to the oxygen adsorption mechanism, the interface state density N_S is related to the concentration of free O distributed at the ZnO grain boundaries. When the Tm_2O_3 content increases from 0.00 to 0.50 mol%, the smaller and more uniform microstructure of the ZnO grains in the

sample makes it easier for free O generated in the ZnO grains to enter the ZnO grain boundary region, capturing electrons near the grain boundaries and forming negatively charged O' and O". The formation of a large number of negatively charged O' and O" at the grain boundaries increases N_S, thereby improving φ_b. Excessive doping (≥ 0.75 mol%) of Tm_2O_3 causes uneven aggregation of the Tm_2O_3 phase, reducing the uniformity of the microstructure, hindering the transfer of O, and thus leading to a decrease in N_S and φ_b.

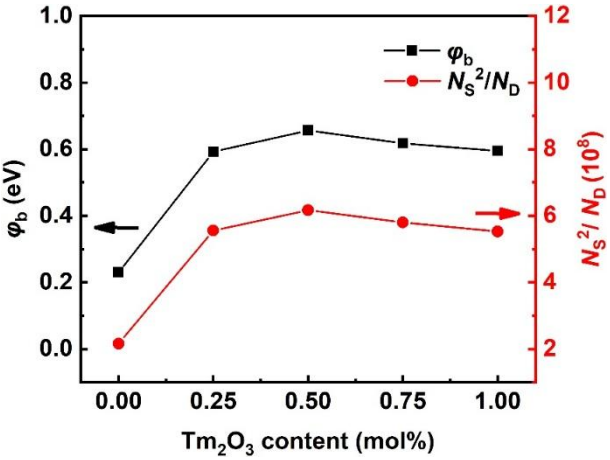


Fig. 8 φ_b-N_S^2/N_D relationship diagram for the samples with different Tm_2O_3 contents.

Table 2 Double Schottky barrier related parameters for the samples with different Tm_2O_3 contents.

Tm_2O_3 (mol%)	φ_b (eV)	N_D ($10^{24}/m^3$)	N_S ($10^{16}/m^2$)	N_S^2/N_D	ρ_{gb} (MΩ·cm)
0.00	0.23	1.11	1.55	2.16	116
0.25	0.59	3.13	4.17	5.56	1417
0.50	0.66	5.25	5.69	6.17	18832
0.75	0.62	2.36	3.70	5.80	1748
1.00	0.59	0.79	2.09	5.53	685

3.5 Impedance characteristics analysis

A Nyquist plot is a graph describing the relationship between the resistance and reactance changes of a material at different frequencies. This study measured the impedance spectra of the samples at room temperature 298.15 K in the frequency range of 200 Hz–2 MHz, and fitted the impedance characteristics using Z-View software. The fitting circuit diagram is shown in Fig.9, where the capacitor C is connected in parallel with the grain resistance R_g, the constant phase element CPE is connected in parallel with the grain boundary resistance R_{gb}, and then the two are connected in series. The complex impedance is determined by Eq. 11 [18, 19, 31]:

$$Z^* = Z' - jZ'' = [\frac{1}{R_g} + j\omega Cg]^{-1} + [\frac{1}{R_{gb}} + P(j\omega)^n]^{-1} \quad (11)$$

where $P(j\omega)^n$ $(0 < n < 1)$ represents the impedance of the CPE element, P is a constant, Cg represents the grain capacitance. When n=0, the CPE is a resistor, and when n=1, the CPE is a capacitor. The grain resistivity ρ_g and grain boundary resistivity ρ_{gb} of the samples were calculated based on the impedance data fitted by Z-View software.

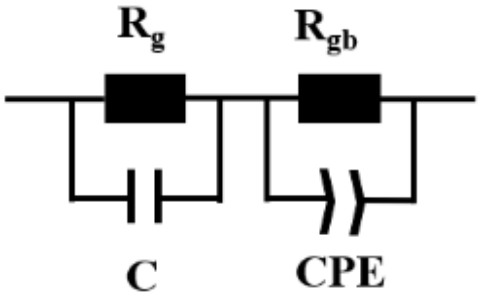


Fig. 9 Fitted impedance circuit diagram of the sample.

Fig. 10a shows the Nyquist plots of the samples with different Tm_2O_3 contents. The grain boundary resistivity ρ_{gb} calculated from these plots is listed in Table 2. Fig. 10b shows the influence trend of Tm_2O_3 content on grain boundary resistivity ρ_{gb}, nonlinear coefficient α, and grain boundary barrier height φ_b. Combining Fig. 6b and Fig. 10b, it can be seen that as the Tm_2O_3 doping amount continuously increases, ρ_{gb}, α, and φ_b all show a trend of first increasing and then decreasing, while the leakage current density J_L first decreases and then increases.

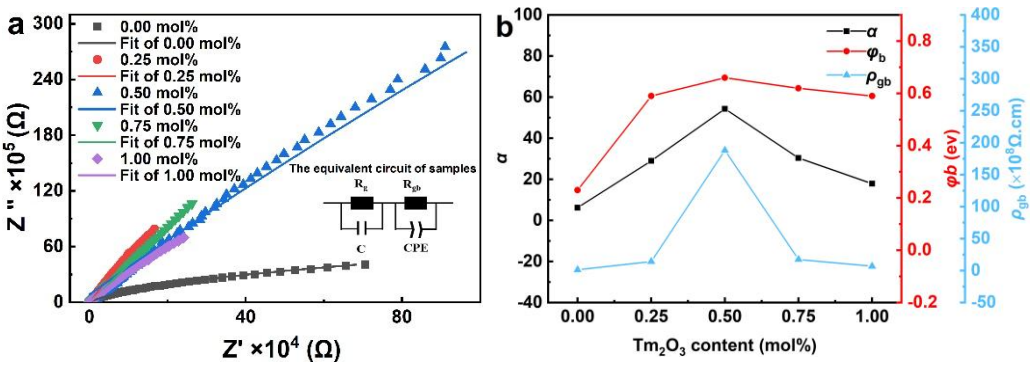


Fig. 10 Nyquist plots and equivalent circuits of the samples with different Tm_2O_3 contents in the frequency range of 200 Hz - 2 MHz (a) and the relationship diagrams of nonlinearity coefficient, grain boundary barrier height and grain boundary resistivity (b).

When the Tm_2O_3 doping amount increases from 0.00 to 0.50 mol%, the grain boundary barrier height φ_b gradually increases. Electrons need to overcome a higher energy barrier to pass through the grain boundaries, resulting in an enhanced blocking effect of the grain boundaries on the current.

Macroscopically, this is manifested as a significant increase in grain boundary resistivity ρ_{gb} and a continuous decrease in leakage current density J_L. The continuously increasing φ_b and ρ_{gb} cause the current to be strongly suppressed under low electric fields (high resistance state), when the breakdown voltage is reached, the current increases sharply (low resistance state) due to the avalanche breakdown mechanism of the double Schottky barrier. This sharp transition from the high resistance state to the low resistance state leads to a continuous increase in the nonlinear coefficient α. As the Tm_2O_3 doping amount increases from 0.50 to 1.00 mol%, the grain boundary barrier height φ_b gradually decreases, leading to a significant reduction in grain boundary resistivity ρ_{gb}, a continuous increase in leakage current density J_L, and a subsequent gradual decrease in nonlinear coefficient α. In summary, appropriate Tm_2O_3 doping (0.50 mol%) significantly increases the grain boundary barrier height φ_b by optimizing the grain boundary phase composition and microstructure, which macroscopically manifests as a tremendous increase in grain boundary resistivity ρ_{gb}. It directly leads to a significant reduction in leakage current density J_L and a substantial increase in nonlinear coefficient α. Excessive doping leads to performance degradation due to the deterioration of the Tm_2O_3 phase distribution, causing a decrease in φ_b and ρ_{gb}.

3.6 Dielectric properties

Fig. 11a shows the variation of the relative permittivity ε′ with frequency *f* for the samples with different Tm_2O_3 contents. For all samples, the relative permittivity ε' continuously decreases as the test frequency increases from 200 Hz to 2 MHz. Near the frequency of about 10^5 Hz, ε' shows a distinct rapid decrease, after which the rate of decrease slows down. This behavior is a typical characteristic of interfacial polarization (Maxwell-Wagner-Sillars, MWS polarization) in polycrystalline ceramics. In ZnO varistors, conductive ZnO grains are separated by highly resistive grain boundary layers, forming a "resistor-capacitor (R-C)" like network. At low frequencies, interfacial charges have sufficient time to accumulate and dissipate at the grain boundaries following the alternating electric field, producing strong interfacial polarization and contributing to a large ε' value. As the frequency increases, the migration of interfacial charges gradually fails to keep up with the change speed of the electric field, leading to a reduction in the polarization contribution and a decrease in ε'. The inflection point frequency corresponds to the main interfacial polarization relaxation process. It is worth noting that the sample doped with 0.50 mol% Tm_2O_3 has the lowest ε'

value over the entire frequency range, which is closely related to its highest grain boundary resistivity ρ_{gb} and barrier height φ_b. The highly resistive grain boundaries limit the migration and accumulation of interfacial charges, weakening the interfacial polarization strength.

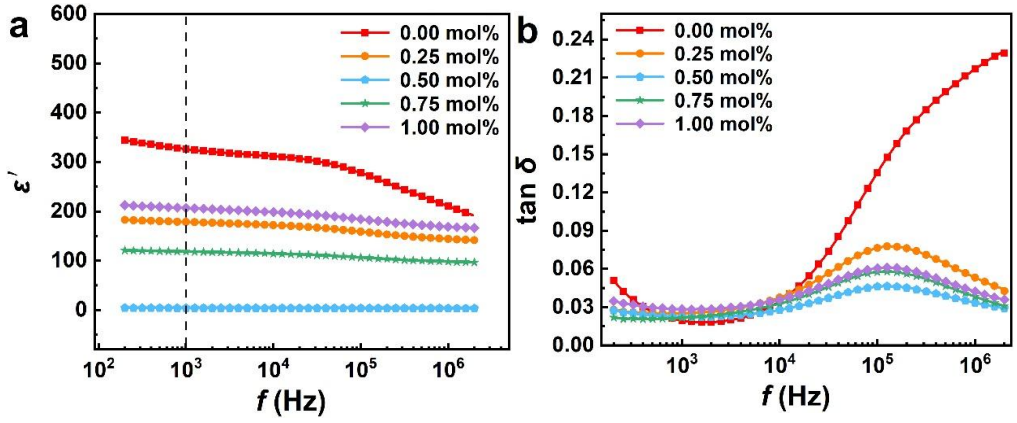


Fig. 11 The frequency f dependence of relative permittivity ε' (a) and loss tangent tanδ (b) for the samples with different Tm_2O_3 contents.

Fig. 11b shows the variation of the loss tangent tanδ with frequency f for the samples with different Tm_2O_3 contents. From Fig. 10b, it can be observed that near a frequency of about 0.1 MHz, all doped samples show a distinct loss peak, and the position of this peak corresponds to the inflection point frequency of the rapid decrease in ε' in Fig. 11a. Tm_2O_3 doping significantly reduces tanδ. This is mainly attributed to two aspects: On one hand, the increase in grain boundary barrier height φ_b and resistivity ρ_{gb} greatly suppresses the leakage conduction current, and leakage conduction loss usually dominates in the low-frequency region, leading to a reduction in tanδ near 200 Hz. On the other hand, the optimized grain boundary structure and phase composition may reduce the concentration or mobility of mobile charge carriers at the interface, thereby weakening the polarization loss and relaxation loss caused by the migration of these charge carriers, leading to a reduction in tanδ near 0.1 MHz. The 0.50 mol% sample has the lowest leakage current J_L and the highest φ_b and ρ_{gb}, so its lowest tanδ is as expected [32]. When the Tm_2O_3 content exceeds 0.50 mol%, although tanδ is still lower than that of the undoped sample, it increases relative to the 0.50 mol% sample. It is related to the excessive aggregation and uneven distribution of the Tm_2O_3 phase at the grain boundaries, leading to a decrease in φ_b and ρ_{gb}, an increase in leakage current J_L, and the introduction of new defect states, which increases the dielectric loss.

The dielectric performance analysis further corroborates the key regulatory role of Tm_2O_3 doping on grain boundary characteristics. Appropriately doping Tm_2O_3 into ZnO-Cr_2O_3-based varistors can effectively suppress interfacial polarization and leakage conduction loss by increasing the grain boundary barrier and resistivity, significantly reducing the dielectric constant ε′ and the loss factor tanδ. The improvement in low-frequency loss is particularly important for device stability.

4 Conclusion

In this work, Tm_2O_3-doped (0.00–1.00 mol%) ZnO-Cr_2O_3-based varistors were prepared using the solid-state reaction method and the correlation mechanism between their microstructure and electrical properties was investigated systematically. XRD and SEM analyses indicate that the introduction of Tm_2O_3 is mainly segregated at the grain boundaries, forming a second phase Tm_2O_3 that inhibits grain boundary migration through a pinning effect, continuously reducing the average grain size from 3.16 to 1.37 μm as the doping amount increases from 0.00 to 0.50 mol%. This grain refinement effect directly increases the number of grain boundaries per unit thickness, forming the structural basis for the leap in voltage gradient strength E_{1mA} from 428.37 to 1778.33 V/mm. Further EDS and barrier analysis show that the selective enrichment of Co element in the grain boundary Tm_2O_3 phase increases the interface state density N_S from 1.55×10^{16} to 5.69×10^{16} m^{-2}, thereby driving the grain boundary barrier height φ_b to increase from 0.23 to 0.66 eV. The increase in barrier height directly enhances the blocking ability of grain boundaries to electrons, causing the nonlinear coefficient α to increase significantly from 6.22 to 54.36, while significantly suppressing the leakage current density J_L from 375.75 to 0.97 μA/cm². The grain boundary resistivity ρ_{gb} also correspondingly increases to 18832 MΩ·cm. However, when the doping amount exceeds 0.50 mol%, the excessive aggregation of the Tm_2O_3 phase destroys the uniformity of the grain boundaries, leading to a weakened pinning effect a rebound in grain size (increasing to 1.71 μm), and a decrease in barrier height (dropping to 0.59 eV), ultimately causing a decrease in voltage gradient strength and deterioration of nonlinear characteristics. This study confirms that the synergistic mechanism of grain refinement to increase the voltage gradient strength and barrier elevation to enhance the nonlinear coefficient and suppress leakage current is the key to achieving high-performance ZnO-Cr_2O_3-based varistors with appropriate Tm_2O_3 doping (0.50 mol%).

Author contributions

Wenbin Cao: Conceptualization, Methodology, Writing - review & editing. **Huitao Wang**: Data curation, Writing - original draft. **Chenyuan Gou**: Investigation, Data curation. **Xinyao Wang**: Data curation. **Jianke Liu**: Conceptualization, Writing - review & editing. **Mingxia Li**: Data curation.

Funding

This work was supported by the National Natural Science Foundation of China (51802183).

Data availability

The data used to support the findings of this study are available from the corresponding author upon request.

Declarations

The authors declare that they have no known competing financial interests or personal relationships that could have appeared to influence the work reported in this paper.

References

[1] S. Bernik, P. Zupančič, D. Kolar, Influence of Bi_2O_3/TiO_2, Sb_2O_3 and Cr_2O_3 doping on low-voltage Varistors, J. Eur. Ceram. Soc. 19 (1999) 709-713.

[2] J. Li, S. Luo, M.A. Alim, The role of TiO_2 powder on the $SrTiO_3$-based synthesized varistor materials, Mater. Lett. 60 (2006) 720-724.

[3] J. Tian, Y. Wu, H. Tian, et al., Microstructure and nonlinear electrical properties in Na_2CO_3-ZnO Varistors, Mater. Sci. Eng. B 300 (2024) 117084.

[4] Y. Tu, Z. Zheng, X. Li, AC aging characteristics of ZnO varistors regulated by Co doping (in Chinese), Sci. Sin. Technol.

[5] Z. Chen, Zinc Oxide Varistors and Its Application in Power Systems (in Chinese), Water Resources and Electric Power Press, Beijing, 1992.

[6] K. Kang, Study on Ge-GeO_2 doped TiO_2 based Varistors (in Chinese), Master Thesis, Kunming University of Science and Technology, Kunming, 2016.

[7] Q. Yan, Preparation and mechanism of rare-earth oxides and nano-ZnO doped varistor materials (in Chinese), Ph.D. Thesis, Sichuan University, Chengdu, 2003.

[8] P. Meng, X. Zhao, Z. Fu, et al., Novel zinc-oxide varistor with superior performance in voltage gradient and aging stability for surge arrester, J. Alloys Compd. 789 (2019) 948-952.
[9] K. Hembram, T.N. Rao, M. Ramakrishna, et al., A novel economical grain boundary engineered ultra-high performance ZnO varistor with lesser dopants, J. Eur. Ceram. Soc. 38 (2018) 5021-5029.
[10] W. Liu, L. Zhang, F. Kong, et al., Enhanced voltage gradient and energy absorption capability in ZnO Varistors by using nano-sized ZnO powders, J. Alloys Compd. 808 (2020) 154252.
[11] M. Zhao, X. Li, Y. Shi, et al., Using semi-finished Ce-La extracts as the sole RE source to synthesize high-performance ZnVMnNbO Varistors, Ceram. Int. 44 (2018) 6912-6917.
[12] P. Meng, S. Lyu, J. Hu, et al., Tailoring low leakage current and high nonlinear coefficient of a Y-doped ZnO varistor by indium doping, Mater. Lett. 188 (2017) 77-79.
[13] T. Tian, L. Zheng, M. Podlogar, et al., Novel ultrahigh-performance ZnO-based Varistors, ACS Appl. Mater. Interfaces 13 (2021) 35924-35929.
[14] T. Tian, L. Zheng, S. Bernik, et al., Influence of Cr_2O_3 doping on the electrical characteristics of novel ZnO-Cr_2O_3-based Varistors, Mater. Res. Bull. 159 (2023) 112111.
[15] T. Tian, G. Li, S. Bernik, et al., Effect of Co_3O_4-doping on the microstructure and electrical properties of novel ZnO-Cr_2O_3-based varistor, J. Eur. Ceram. Soc. 42 (2022) 2268-2273.
[16] T. Tian, L. Zhang, M. Podlogar, Z. Man, X. Ruan, X. Shi, Influence of Ca-doping on the nonlinear properties of novel ZnO-Cr_2O_3-based Varistors, J. Eur. Ceram. Soc. 42 (2022) 2268-2273.
[17] J. Su, Study on preparation and properties of lanthanide oxide doped Zn-Bi based Varistors (in Chinese), Master Thesis, Shaanxi University of Science & Technology, Xi'an, 2022.
[18] W. Cao, C. Gou, J. Liu, et al., High performance Eu_2O_3-doped ZnO-Cr_2O_3-based varistors with high breakdown field strength and excellent aging resistance, Ceram. Int. (2025).
[19] C. Gou, W. Cao, J. Liu, Er_2O_3 doped ZnO-Cr_2O_3-based varistors with high voltage gradient, Ceram. Int. 50 (2024) 37761-37770.
[20] W. Cao, C. Gou, S. Liu, et al., Effect of Oxygen Vacancy on Improving the Properties of ZnO-Bi_2O_3-Based Varistors, J. Electron. Mater. 53 (2024) 8118-8125.
[21] L. Wang, N. Zhao, J. Su, Electrical properties of Er_2O_3 doped ZnO Varistors (in Chinese), J. Chin. Ceram. Soc. 51 (2023) 3059-3066.
[22] W. Cao, X. Xie, Y. Wang, et al., Effect of Pr_6O_{11} doping on the microstructure and electrical properties of ZnO varistors, Ceram. Int. 45 (2019) 24777-24783.
[23] S. Wan, Study on low-temperature sintering of low-voltage ZnO varistors and fabrication of chip varistors by aqueous tape casting (in Chinese), Ph.D. Thesis, Huazhong University of Science and Technology, Wuhan, 2010.

[24] J. Liu, X. Luo, W. Cao, et al., Influence of Co_2O_3 doping on the microstructure and electrical properties of ZnO-Bi_2O_3-based varistors, Mater. Sci. Semicond. Process. 153 (2023) 107179.

[25] J. Liu, J. Zhu, W. Cao, et al., Effect of Sc_2O_3 doping on microstructure and electrical properties of ZnO-Bi_2O_3-based varistors, Phys. B Condens. Matter 650 (2023) 414552.

[26] W. Cao, N. Zhao, J. Su, et al., Bi-Er-O pre-synthesized phase $(Bi_{1-x}Er_x)_2O_3$ doped ZnO varistors with high nonlinear coefficient and low leakage current, Ceram. Int. 50 (2024) 22077-22084.

[27] J. Liu, X. Luo, W. Cao, Effect of Sc_2O_3 doping on the microstructure and electrical characteristics of ZnO linear resistors, J. Alloys Compd. 946 (2023) 169445.

[28] J. Liu, B. Ren, W. Cao, Preparation and electrical properties of Eu_2O_3 doped high-performance ZnO-Bi_2O_3 based varistors, Ceram. Int. (2025).

[29] L. Zhou, Y. Liu, H. Chen, Improving properties of ZnO-Bi_2O_3 based Varistors by two-step sintering (in Chinese), J. Shaanxi Univ. Sci. Technol. (2023) 1-8.

[30] D. Wang, More thoughts on X-ray diffraction experiments (in Chinese), Technol. Wind (2021) 62–63.

[31] Z. Fu, J. He, J. Lu, et al., Investigation of dielectric relaxation and degradation behavior of two-step sintered ZnO varistors, Ceram. Int. 45 (2019) 21900-21909.

[32] F. Cui, Z. Xu, R. Chu, et al., Low temperature sintering ZnO-Bi_2O_3 based Varistors with low electrical breakdown voltage and high nonlinear coefficient, Ceram. Int. 47 (2021) 4118-4126.

[33] K. Wang, Preparation and electrical properties of high voltage ZnO varistors (in Chinese), Master Thesis, Xidian University, Xi'an, 2019.

[34] C.-W. Nahm, Microstructure, electrical properties, and dc aging characteristics of Tb_4O_7-doped ZnO-based varistors, J. Mater. Sci. 43 (2008) 2857-2864.

[35] C.-W. Nahm, Effect of sintering temperature on nonlinear electrical properties and stability against DC accelerated aging stress of (CoO, Cr_2O_3, La_2O_3)-doped ZnO-Pr_6O_{11}-based varistors, Mater. Lett. 60 (2006) 3311-3314.